

Fast relaxation on magnetic-dipole-forbidden spin transitions of nitrogen-vacancy centers in nanodiamonds

A. Gardill,* M. C. Cambria,* and S. Kolkowitz[†]

Department of Physics, University of Wisconsin, Madison, Wisconsin 53706, USA

(Dated: July 19, 2022)

Thanks to their versatility, nitrogen-vacancy (NV) centers in nanodiamonds have been widely adopted as nanoscale sensors. However, their sensitivities are limited by their short coherence times relative to NVs in bulk diamond. A more complete understanding of the origins of decoherence in nanodiamonds is critical to improving their performance. Here we present measurements of fast spin relaxation on magnetic-dipole-forbidden transitions between the $m_s = |\pm 1\rangle$ spin states of the NV^- electronic ground state in ~ 40 -nm nanodiamonds under ambient conditions. For frequency splittings between the $|\pm 1\rangle$ states of ~ 20 MHz or less the maximum achievable coherence time of the NV spin is ~ 2 orders of magnitude shorter than would be expected based on the lifetime of the $m_s = |0\rangle$ state. We attribute this fast relaxation to electric field noise. We observe a strong falloff of the relaxation rate with the splitting between $|\pm 1\rangle$, suggesting that, whenever possible, measurements with NVs in nanodiamonds should be performed at moderate axial magnetic fields (> 60 G). We also observe that the relaxation rate changes with time. These findings indicate that surface electric field noise is a major source of decoherence for NVs in nanodiamonds.

Nitrogen-vacancy (NV) centers in diamond have a number of properties that make them attractive candidates for use as quantum sensors. The NV^- ground-state electronic spin triplet can be optically polarized and read-out via fluorescence, exhibits millisecond-long coherence times at room temperature in bulk diamond [1–4], and can be used as a probe of the local magnetic [5], electric [6, 7], strain [8, 9], and thermal [10, 11] environments. NVs in diamond nanocrystals, or nanodiamonds, are particularly attractive for sensing applications as they can be functionalized [12], placed at the ends of scanning tips [5, 13], deterministically positioned on nanophotonic structures [14, 15], optically levitated [16, 17], or even inserted into living cells [10]. Unfortunately, the coherence times of the electronic spins of NVs in commercial nanodiamonds are consistently on the order of $\sim 1 - 10$ microseconds [3, 18], $\sim 2 - 3$ orders of magnitude shorter than what is regularly achieved with NVs in bulk diamond [1–4], limiting their sensitivities for many applications. There have been a number of efforts to improve the coherence times of NVs in nanodiamonds, including milling from high purity bulk diamond [19], high temperature annealing [20], dynamical decoupling [19, 21], and a variety of surface treatments [18, 22, 23], but thus far only marginal improvements have been observed. A better understanding of the origins of decoherence in nanodiamonds is required to unlock their full potential.

Prior efforts to improve the coherence times of NVs in nanodiamonds have focused on magnetic noise as the primary source of both dephasing and relaxation [18, 19, 21–23]. However, in a recent work Myers *et al.* found that in shallow NVs ~ 7 nm away from the surface in bulk diamond, electric field noise emanating from the surface can drive magnetic-dipole-forbidden transitions with $\Delta m_s = 2$ between the $m_s = |\pm 1\rangle$ states, sometimes called double quantum transitions, at rates up to

~ 2 kHz, or more than $20\times$ the rate between the $m_s = |0\rangle$ state and the $|\pm 1\rangle$ states [24]. As NVs in nanodiamonds are tens of nanometers away from the surface in all directions and the surfaces are more difficult to control than those of bulk diamond samples, it is natural to ask whether this effect occurs in nanodiamonds as well. Here we present measurements indicating that relaxation on magnetic-dipole-forbidden transitions is a dominant source of decoherence for NVs in ~ 40 -nm commercial nanodiamonds under ambient environmental conditions.

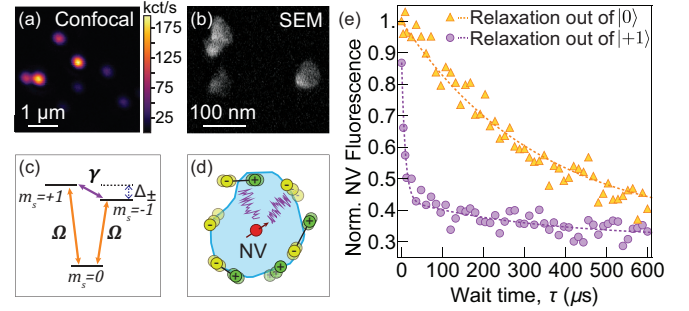


FIG. 1. Fast relaxation on magnetic-dipole-forbidden spin transitions of NVs in nanodiamonds. (a) Confocal microscope image of NV centers in nanodiamonds. (b) Scanning electron microscope (SEM) image of three nanodiamonds. (c) Ground state level-structure of the NV^- . Magnetic-dipole-allowed transitions between $|0\rangle \leftrightarrow |\pm 1\rangle$ occur at rate Ω , and magnetic-dipole-forbidden transitions between $|+1\rangle \leftrightarrow |-1\rangle$ at rate γ . (d) Diagram of a single NV in a nanodiamond. Moving charges or fluctuating electric dipoles create electric field noise (purple lines) that drive NV spin relaxation. (e) Measurement of state dependent population relaxation. Relaxation out of $|0\rangle$ (orange triangles) exhibits a single exponential with rate 3Ω . Relaxation out of $|+1\rangle$ (purple circles) exhibits a biexponential decay that depends on both Ω and γ (dashed purple line). Dashed lines are Eqs. 1, 2, and account for π -pulse infidelities, with $\Omega = 1.0$ kHz, $\gamma = 56$ kHz.

At low axial magnetic fields, $B_z < 10$ G, we find that the rate of magnetic-dipole-forbidden transitions between the $|\pm 1\rangle$ states can exceed 100 kHz, more than two orders of magnitude faster than the rate between the $|0\rangle$ and $|\pm 1\rangle$ states, limiting the maximum achievable coherence times of these NVs to tens of microseconds. We attribute this to electric field noise that drives the transitions between the $|\pm 1\rangle$ states. We observe this behavior in all 5 of the single NVs in nanodiamonds that we studied. We characterize the dependence of this rate on the frequency splitting, Δ_{\pm} between the $|\pm 1\rangle$ states and observe a strong falloff with Δ_{\pm} , consistent with a $1/f^2$ scaling of the noise power spectral density. This indicates that, whenever possible, coherent measurements with nanodiamonds should be performed with moderate magnetic fields (> 60 G) applied along the NV axis. Finally, we observe fluctuations in this relaxation rate on hour to day time-scales, which we consider to be a strong indication that the noise is emanating from the nanodiamond surface.

Our experimental setup consists of a room temperature confocal microscope. All data was taken with commercial nanodiamonds from Adámas Nano with a mean diameter of 40 nm and an average of 1 - 4 NVs per nanocrystal, spin coated onto a thin glass coverslip. The nanodiamond surfaces were untreated. A fluorescence image of single NVs in nanodiamonds is shown in Fig. 1a, along with a scanning electron microscope (SEM) image of nanodiamonds from the same suspension in Fig. 1(b). Before measuring relaxation rates, we select nanodiamonds containing only single NVs determined by second-order photon correlation measurements [25]. We then select NVs with spin-dependent fluorescence contrasts greater than $\sim 10\%$ at low magnetic fields. In total, we identified 5 NVs out of a starting set of 110 that met these criteria.

As shown in Fig. 1(c), the NV electronic ground state is a spin-triplet. In most NV studies and applications, a d.c. magnetic field (B_z) is applied along the NV axis to lift the degeneracy between the $|\pm 1\rangle$ states, and the NV is then treated as a two-level system with a spin lifetime T_1 found by measuring the lifetime of the $|0\rangle$ state. Figure 1(e) shows representative population decay curves for the spin states $|0\rangle$ and $|+1\rangle$ of an NV in a nanodiamond. At low B_z , population prepared and readout in $|+1\rangle$ exhibits a biexponential decay and has mostly depolarized after just ~ 20 microseconds (purple circles). However, the standard T_1 measurement employed in almost all NV studies, which consists of optically polarizing in $|0\rangle$, waiting some time τ , and measuring the population in $|0\rangle$ via fluorescence, exhibits a single exponential decay with a much longer time-constant of ~ 330 microseconds (orange triangles). Critically, this measurement is blind to the population leakage between $|+1\rangle$ and $|-1\rangle$, and would therefore drastically overestimate the achievable coherence time T_2 for this NV.

Figure 2(a) illustrates the measurement sequence we

use to measure the population dynamics into and out of each of the three spin states [24, 26, 27]. Preparation and readout of any of the three states is achieved by using a combination of 532 nm optical polarization and state-selective resonant microwave π -pulses, allowing for a total of nine measurement combinations [25]. For example, Figure 2(b) shows the sequence used to prepare in $|+1\rangle$ and measure the population in $|-1\rangle$. After the population is optically polarized into $|0\rangle$, a microwave π_+ -pulse transfers the population to $|+1\rangle$. After a wait time τ , a π_- -pulse swaps the populations in $|-1\rangle$ and $|0\rangle$. The transferred population of the state $|-1\rangle$ is then readout out via fluorescence under 532 nm illumination and normalized to a reference measurement of the NV brightness when it has been polarized in the $|0\rangle$ state. The purple circles in Fig. 1(e) correspond to using this sequence to prepare in $|+1\rangle$, wait, and then readout in $|+1\rangle$.

Figure 2(c) shows a measurement of the population dy-

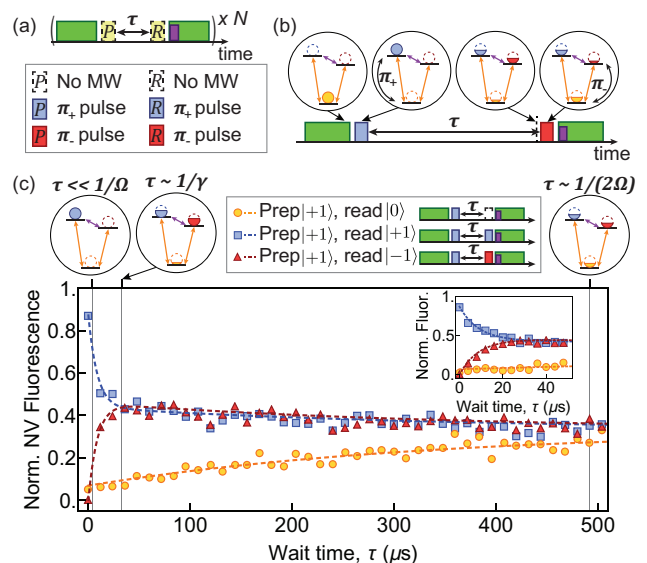


FIG. 2. State-selective population relaxation measurements. (a) The measurement sequence consists of preparing NV in $|\pm 1\rangle$ or $|0\rangle$, waiting time τ , and reading out the population of $|\pm 1\rangle$ or $|0\rangle$. Sequences are repeated $N \sim 10^5$ times. Preparation and readout of population in $|0\rangle$ is achieved using 532 nm optical illumination (green rectangles) and fluorescence readout (purple rectangle), while state-selective microwave π -pulses transfer population into and out of $|\pm 1\rangle$ (red and blue rectangles). (b) Example of single measurement sequence of preparation in $|+1\rangle$ and readout in $|-1\rangle$. (c) Representative population dynamics for a single NV in a nanodiamond prepared in $|+1\rangle$, with $\Delta_{\pm} = 28.9(6)$ MHz. The population in states $|+1\rangle$ (blue squares), $|-1\rangle$ (red triangles), and $|0\rangle$ (yellow circles) after wait time τ are measured by the method explained in (a) and (b). Dashed colored lines are solutions to the three level population dynamics equations, accounting for π -pulse infidelities, with $\Omega = 1.0$ kHz, $\gamma = 56$ kHz. Inset shows population dynamics of same NV over first 50 μ s of relaxation.

namics of the three spin states after preparation in $|+1\rangle$ for a representative NV at a splitting of $\Delta_{\pm} = 28.9(6)$ MHz. The fast relaxation out of $|+1\rangle$ into $|-1\rangle$ is readily apparent. Remarkably, the population in $|-1\rangle$ is non-monotonic with time, as the population prepared in $|+1\rangle$ first rapidly decays to an even mixture of $|\pm 1\rangle$ before slowly decaying into an unpolarized mixture of all three spin states.

To capture the full population dynamics, we solve the rate equations for a generic three-level system with arbitrary transition rates between each pair of states. Empirically, we find that the transition rates for $|0\rangle \leftrightarrow |+1\rangle$ and $|0\rangle \leftrightarrow |-1\rangle$ are equivalent to within our measurement uncertainties [25], which simplifies the analysis. Using the rates as defined in Fig. 1(c), and assuming the NV states are in S_z eigenstates ($|0\rangle, |\pm 1\rangle$), the population equations for the three NV states are given by [24, 26, 28]

$$\rho_0(\tau) = \frac{1}{3} + \left(\rho_0(0) - \frac{1}{3}\right) e^{-3\Omega\tau}, \quad (1)$$

$$\rho_{\pm 1}(\tau) = \frac{1}{3} \pm \frac{1}{2} \Delta\rho_{\pm 1}(0) e^{-(2\gamma+\Omega)\tau} - \frac{1}{2} \left(\rho_0(0) - \frac{1}{3}\right) e^{-3\Omega\tau}, \quad (2)$$

where τ is the wait time, $\rho_{0,\pm 1}(\tau)$ are the populations of the $|0, \pm 1\rangle$ states at time τ , $\rho_0(0)$ is the initial population of $|0\rangle$, and $\Delta\rho_{\pm 1}(0)$ is the difference in the initial population of $|+1\rangle$ and $|-1\rangle$. The dashed colored lines in Fig. 1(e) and 2(c) are plots of Eqs. 1 and 2, accounting for measured π -pulse infidelities [25]. We observe excellent agreement between this model and all of the relaxation measurements we performed.

We note that as a result of intrinsic d.c. strain or electric fields, at low magnetic fields the spin eigenstates are the bright and dark states $|\pm\rangle = (|+1\rangle \mp e^{-i\phi_{\Pi\perp}} |-1\rangle) / \sqrt{2}$, where $\phi_{\Pi\perp}$ is the angle of the electric/strain field in the plane transverse to the NV axis [7]. However, in this case the same arguments, measurements, and equations presented above apply with the states $|\pm 1\rangle$ replaced by the states $|\pm\rangle$ [25].

To extract values for the transition rates γ and Ω , we follow the analysis protocol laid out in [24]. We denote the time-dependent populations we measure in state $|j\rangle$ after initial preparation in $|i\rangle$ with $P_{i,j}(\tau)$. From Eqs. 1 and 2, subtracting $P_{0,0}(\tau)$ and $P_{0,+1}(\tau)$ gives

$$F_{\Omega}(\tau) = P_{0,0}(\tau) - P_{0,+1}(\tau) = ae^{-3\Omega\tau}, \quad (3)$$

where a is the fluorescence contrast between the two subtracted data sets. Similarly, subtracting $P_{+1,+1}(\tau)$ and $P_{+1,-1}(\tau)$ results in

$$F_{\gamma}(\tau) = P_{+1,+1}(\tau) - P_{+1,-1}(\tau) = ae^{-(2\gamma+\Omega)\tau}. \quad (4)$$

This method allows us to fit a single exponential to each subtracted set and isolate the rates Ω and γ . For all

5 NVs we observe $\gamma \gg \Omega$ at low axial magnetic fields. Characteristics of each NV are summarized in Table I.

Figure 3 shows the relaxation rates γ and Ω as a function of the frequency splitting Δ_{\pm} for 4 of the NVs measured (similar rates and scalings were also observed for the 5th NV, see [25]). The rate γ initially decreases rapidly with increasing Δ_{\pm} while Ω appears constant over the measured range $B_z \sim 0-200$ G. Similar to the results for shallow NVs in bulk diamond [24], the scaling is relatively well described by $\gamma(\Delta_{\pm}) = A_0/\Delta_{\pm}^2 + \gamma_{\infty}$ (dashed purple lines), where A_0 and γ_{∞} are constants.

To discuss the origins of the observed fast transitions between $|+1\rangle$ and $|-1\rangle$, we introduce the NV ground-state Hamiltonian. Ignoring hyperfine coupling, the Hamiltonian [29] can be expressed as a sum of the zero-field splitting D_{gs} , the interaction with magnetic field \mathbf{B} , and the interaction with electric and scaled strain field $\mathbf{\Pi}$. That is (with $\hbar = 1$),

$$H = H_{zfs} + H_B + H_{\Pi}, \quad (5)$$

where

$$H_{zfs} = D_{gs} S_z^2, \quad (6)$$

$$H_B = g\mu_B \mathbf{B} \cdot \mathbf{S}, \quad (7)$$

$$H_{\Pi} = d_{\parallel} \Pi_z S_z^2 + d'_{\perp} \Pi_x (S_x S_z + S_z S_x) + d'_{\perp} \Pi_y (S_y S_z + S_z S_y) + d_{\perp} \Pi_x (S_x^2 - S_y^2) + d_{\perp} \Pi_y (S_x S_y + S_y S_x).$$

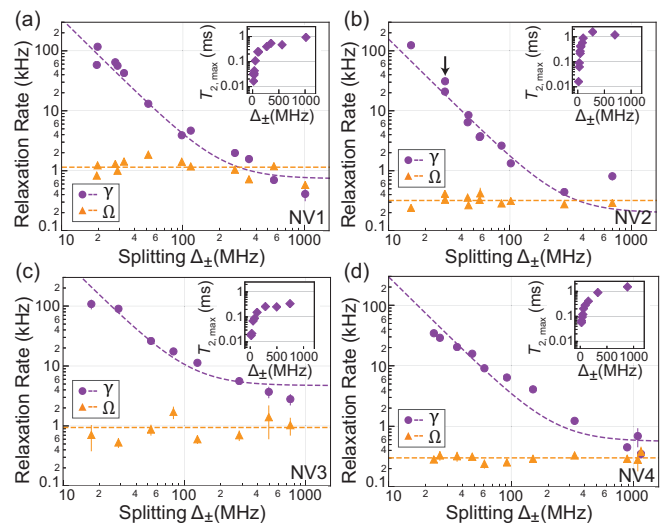


FIG. 3. Dependence of relaxation rates γ and Ω on the frequency splitting between $|\pm 1\rangle$ states, Δ_{\pm} , for four separate NVs. Purple circles represent measurement of γ , orange triangles represent measurement of Ω . A fit to $\gamma(\Delta_{\pm}) = A_0/\Delta_{\pm}^2 + \gamma_{\infty}$ is shown on all four plots (dashed purple lines). Error bars are twice the standard error. The point in (b) marked by a black arrow is referenced in Fig. 4. Insets show the corresponding maximum achievable $T_{2,\max}$ (purple diamonds) based on Eq. 9 on a semi-log plot.

TABLE I. Characteristics of the five measured NVs. For each NV, the maximum γ we observed is reported with the corresponding splitting Δ_{\pm} and the resulting $T_{2,\max}$. The calculated average Ω_{avg} , γ_{∞} , and A_0 for each NV are also listed (see Fig. 3), along with the measured Δ_{\pm} in the absence of any applied magnetic field. Reported error is twice the standard error.

	Max γ (kHz)	Δ_{\pm} (MHz)	$T_{2,\max}$ (μs)	Ω_{avg} (kHz)	γ_{∞} (kHz)	A_0 (MHz ² ·kHz)	Zero field Δ_{\pm} (MHz)
NV1	117(8)	19.8(6)	16.6(11)	1.1(3)	0.74(6)	$33.9(6)\times 10^3$	19.5(6)
NV2	124(6)	15.3(6)	16.0(8)	0.32(13)	0.20(3)	$15.7(2)\times 10^3$	15.3(6)
NV3	110(20)	17.1(6)	18(3)	1.0(10)	4.7(4)	$59(3)\times 10^3$	15.4(6)
NV4	35(3)	23.4(6)	57(4)	0.30(18)	0.56(4)	$29.4(6)\times 10^3$	23.4(6)
NV5	240(50)	10.9(6)	8.3(17)	0.7(6)	3.7(5)	$18.7(18)\times 10^3$	6.9(6)

Here, \mathbf{S} is the vector of spin-1 operators, $D_{gs}/2\pi = 2.87$ GHz is the zero-field splitting between $|0\rangle$ and $|\pm 1\rangle$, $g\mu_B/2\pi = 2.8$ MHz/G is the NV electronic spin gyromagnetic ratio, and d_{\parallel} , d_{\perp} , and d'_{\perp} are electric dipole parameters with measured values $d_{\parallel}/2\pi = 0.35$ Hz cm/V and $d_{\perp}/2\pi = 17$ Hz cm/V [30]. To our knowledge, d'_{\perp} has not been measured, but *ab initio* studies suggest d'_{\perp} and d_{\perp} may have similar values [29]. However, because the d'_{\perp} terms mix states with energy splitting $\sim D_{gs}$, for weak electric fields d'_{\perp} is frequently taken to be zero [29, 30]. Importantly for this work, $\langle -1|H_B|+1\rangle = 0$, indicating that the $|-1\rangle \leftrightarrow |+1\rangle$ transition is magnetic-dipole-forbidden. However, $\langle -1|H_{\Pi}|+1\rangle$ is nonzero, meaning that the $|-1\rangle \leftrightarrow |+1\rangle$ transition can be driven by electric fields and strain noise. The ability of electric field and strain noise to drive $|0\rangle \leftrightarrow |\pm 1\rangle$ transitions depends upon the value of d'_{\perp} .

Based on the above considerations, we attribute the fast γ relaxation rates to resonant electric field noise at the frequency Δ_{\pm} incoherently driving transitions between $|\pm 1\rangle$ through the d_{\perp} terms in Eq. 8 [25]. While our measurements cannot discriminate between strain and electric field noise, based on our observations of the noise changing in time as described below, and guided by other works where electric field noise emanating from surfaces was observed with NVs [24, 27, 31, 32] and in other materials systems [33–36], we argue that the observed noise is primarily electric field noise emanating from the nanodiamond surfaces. Under this assumption, the measured relaxation rates are then directly proportional to the perpendicular electric field noise power spectrum: $S_{E_{\perp}}(\omega) = \gamma(\omega)/(d_{\perp}^2/h^2)$ [24, 27, 31]. Using the functions of γ determined in Fig. 3, we integrate $S_{E_{\perp}}(\omega)$ over the range of measured frequencies $\omega \approx 20 - 1000$ MHz and find a lower limit order of magnitude estimate of $E_{\perp}^{RMS} = 10^7$ V/m for all five NVs. For comparison, this value is roughly an order of magnitude larger than the d.c. electric field 20 nm away from a single stationary electron. The $1/f^2$ scaling we observe at lower splittings hints at fluctuating electric dipoles or the motion of charges between charge traps as possible sources of the noise [24, 31, 37]. Additionally, we note that Ω_{avg} and γ_{∞} are of the same order of magnitude for each of the NVs surveyed. This suggests that Ω may also be lim-

ited by resonant electric field noise driving $|0\rangle \leftrightarrow |\pm 1\rangle$ transitions, and provides indirect evidence that $d'_{\perp} \neq 0$.

Critically, because the relaxation between $|\pm 1\rangle$ is an incoherent process, it cannot be echoed away and so sets a hard limit on the achievable coherence time T_2 for an NV spin qubit formed from $|0\rangle$ and either $|+1\rangle$ or $|-1\rangle$ [24] of

$$T_{2,\max} = 2(3\Omega + \gamma)^{-1}. \quad (9)$$

Using the measured values of γ and Ω , this value is plotted as a function of Δ_{\pm} in the insets of Fig. 3. These observations may help to explain the mixed results of prior attempts to use dynamical decoupling to extend the coherence times of NVs in nanodiamonds [3, 19, 21]. They also indicate that, whenever possible, measurements with NVs in nanodiamonds should be performed at axial magnetic fields exceeding ~ 60 G. In addition, the observed $1/f^2$ noise scaling implies that the electric field noise power spectral density is even larger at lower frequencies, and as these slowly fluctuating fields will shift the energies of the $|0\rangle \leftrightarrow |\pm 1\rangle$ transitions through the $d_{\parallel}\Pi_z S_z^2$ term in Eq. 8, low frequency charge noise must be considered as a significant source of dephasing in nanodiamonds. This is consistent with measurements by Jamoneau *et al.* of T_2^* as a function of axial magnetic field performed on a single NV in a nanodiamond [32].

As shown in Fig. 3, at several values for Δ_{\pm} we performed a measurement of γ multiple times and observed deviations well above our standard error. We attribute these deviations to variations in the local electric field noise power spectral density as a function of time. Figure 4 shows the value of γ as a function of time by performing the same measurement repeatedly on NV2 at a constant splitting of ~ 29 MHz. The changes in the rate γ in Fig. 4(a) are well outside of the statistical uncertainty of the measurements, and indicate that γ fluctuates in time over hours to days. Similar fluctuations were observed when the same measurements were performed with NV1 [25], and previously in shallow NVs in bulk diamond [24, 38]. While the origins of these temporal dynamics are presently obscure, they provide additional evidence that the observed noise is primarily from the nanodiamond surfaces, where adsorbates may be coming and going with time.

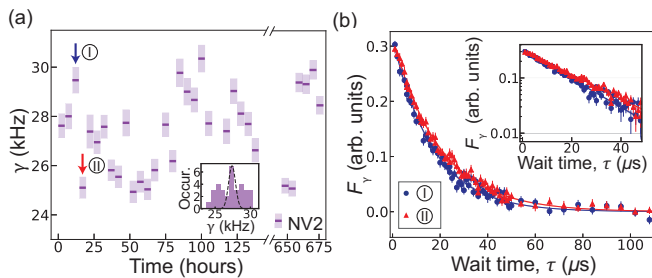


FIG. 4. Temporal fluctuations in the relaxation rate γ . (a) Rate γ of NV2 at a single splitting $\Delta_{\pm} \approx 29$ MHz (referenced by a black arrow in Fig. 3(b)) measured for 140 consecutive hours, followed by a three week long gap, then measured again for 35 consecutive hours. Error bars are one standard error. Inset shows a histogram of the measured rates overlaid with a Gaussian curve with standard deviation equal to the average standard error of the measurements. (b) Measured relaxation curves $F_{\gamma}(\tau)$ (Eq. 4) for the back-to-back measurements labeled in (a), illustrating a change in γ that was well above our signal-to-noise ratio. The inset shows the first 50 μs of the same data plotted on a semi-log scale. Error bars are one standard error.

In conclusion, we have presented observations of fast relaxation rates on magnetic-dipole-forbidden transitions of NV electronic spins in nanodiamonds. We find that this relaxation rate depends on the splitting of the $|\pm 1\rangle$ levels, and that the resulting limit on the coherence time T_2 improves with higher axial magnetic fields. Additionally, we observe this rate changing with time. Our results demonstrate that the magnetic-dipole-forbidden relaxation rate γ between the $|\pm 1\rangle$ states is a critical figure of merit for the coherence of NVs in nanodiamonds, and suggest that electric field noise is a major source of both dephasing and relaxation. Beyond the scope of this work, future experiments could be performed to shed light on the origins of this noise and to develop methods for mitigating it, including studies of how γ changes with surface functionalization, nanodiamond size, immersion in dielectric liquids, or temperature. Additionally, measurements of γ could also be used as a local probe of the electric field noise near surfaces in quantum systems limited by charge noise, such as ion traps [34], semiconductor quantum dots [36], and superconducting qubits [33, 35].

The authors thank Jeff Thompson, Nathalie de Leon, Jeronimo Maze, Ariel Norambuena, Ania Bleszynski Jayich, Mikhail Lukin, Dolev Bluvstein, and Norman Yao for enlightening discussions and helpful insights, and Wangping Ren and Sam Li for their contributions to the experimental apparatus. This work was supported by the U.S. Department of Energy, Office of Science, Basic Energy Sciences under Award #DE-SC0020313. A. G. acknowledges support from the Department of Defense through the National Defense Science and Engineering Graduate Fellowship (NDSEG) program.

* These authors contributed equally.

† kolkowitz@wisc.edu

- [1] G. Balasubramanian, P. Neumann, D. Twitchen, M. Markham, R. Kolesov, N. Mizuochi, J. Isoya, J. Achard, J. Beck, J. Tissler, *et al.*, *Nat. Mater.* **8**, 383 (2009).
- [2] G. De Lange, Z. Wang, D. Riste, V. Dobrovitski, and R. Hanson, *Science* **330**, 60 (2010).
- [3] B. Naydenov, F. Dolde, L. T. Hall, C. Shin, H. Fedder, L. C. L. Hollenberg, F. Jelezko, and J. Wrachtrup, *Phys. Rev. B* **83**, 081201 (2011).
- [4] N. Bar-Gill, L. Pham, A. Jarmola, D. Budker, and R. Walsworth, *Nat. Commun.* **4**, 1743 (2013).
- [5] L. Rondin, J.-P. Tetienne, T. Hingant, J.-F. Roch, P. Maletinsky, V. Jacques, *et al.*, *Rep. Prog. Phys.* **77**, 056503 (2014).
- [6] F. Dolde, H. Fedder, M. W. Doherty, T. Nöbauer, F. Rempp, G. Balasubramanian, T. Wolf, F. Reinhard, L. C. L. Hollenberg, F. Jelezko, J. Wrachtrup, *et al.*, *Nat. Phys.* **7**, 459 (2011).
- [7] T. Mittiga, S. Hsieh, C. Zu, B. Kobrin, F. Machado, P. Bhattacharyya, N. Z. Rui, A. Jarmola, S. Choi, D. Budker, N. Y. Yao, *et al.*, *Phys. Rev. Lett.* **121**, 6 (2018).
- [8] P. Ovartchaiyapong, K. W. Lee, B. A. Myers, and A. C. B. Jayich, *Nat. Commun.* **5**, 4429 (2014).
- [9] J. Teissier, A. Barfuss, P. Appel, E. Neu, and P. Maletinsky, *Phys. Rev. Lett.* **113**, 020503 (2014).
- [10] G. Kucsko, P. C. Maurer, N. Y. Yao, M. Kubo, H. J. Noh, P. K. Lo, H. Park, and M. D. Lukin, *Nature (London)* **500**, 54 (2013).
- [11] D. M. Toyli, C. F. de las Casas, D. J. Christle, V. V. Dobrovitski, and D. D. Awschalom, *P. Natl. Acad. Sci. USA* **110**, 8417 (2013).
- [12] A. Krüger, Y. Liang, G. Jarre, and J. Stegk, *J. Mater. Chem.* **16**, 2322 (2006).
- [13] G. Balasubramanian, I. Chan, R. Kolesov, M. Al-Hmoud, J. Tisler, C. Shin, C. Kim, A. Wojcik, P. R. Hemmer, A. Krueger, *et al.*, *Nature (London)* **455**, 648 (2008).
- [14] S. I. Bogdanov, O. A. Makarova, A. S. Lagutchev, D. Shah, C.-C. Chiang, S. Saha, A. S. Baburin, I. A. Ryzhikov, I. A. Rodionov, A. V. Kildishev, A. Boltasheva, V. M. Shalaev, *et al.*, arXiv:1902.05996 (2019).
- [15] S. Schietinger, M. Barth, T. Aichele, and O. Benson, *Nano Lett.* **9**, 1694 (2009).
- [16] L. P. Neukirch, J. Gieseler, R. Quidant, L. Novotny, and A. N. Vamivakas, *Opt. Lett.* **38**, 2976 (2013).
- [17] T. M. Hoang, J. Ahn, J. Bang, and T. Li, *Nat. Commun.* **7** (2016).
- [18] X. Song, J. Zhang, F. Feng, J. Wang, W. Zhang, L. Lou, W. Zhu, and G. Wang, *AIP Adv.* **4**, 047103 (2014).
- [19] H. S. Knowles, D. M. Kara, and M. Atatüre, *Nat. Mater.* **13**, 21 (2014).
- [20] R. Tsukahara, M. Fujiwara, Y. Sera, Y. Nishimura, Y. Sugai, C. Jentgens, Y. Teki, H. Hashimoto, and S. Shikata, *ACS Appl. Nano Mater.* (2019).
- [21] D.-Q. Liu, G.-Q. Liu, Y.-C. Chang, and X.-Y. Pan, *Physica B* **432**, 84 (2014).
- [22] F. Brandenburg, R. Nagumo, K. Saichi, K. Tahara, T. Iwasaki, M. Hatano, F. Jelezko, R. Igarashi, and T. Yatsui, *Sci. Rep.* **8**, 15847 (2018).

- [23] R. Ryan, A. Stacey, K. M. O'Donnell, T. Ohshima, B. C. Johnson, L. C. L. Hollenberg, P. Mulvaney, and D. A. Simpson, *ACS Appl. Mater. Inter.* **10**, 13143 (2018).
- [24] B. A. Myers, A. Ariyaratne, and A. C. B. Jayich, *Phys. Rev. Lett.* **118**, 7 (2017).
- [25] See supplemental material for experimental details, additional data, and discussion of alternative explanations for the observed fast relaxation.
- [26] S. Kolkowitz, A. Safira, A. A. High, R. C. Devlin, S. Choi, Q. P. Unterreithmeier, D. Patterson, A. S. Zibrov, V. E. Manucharyan, H. Park, M. D. Lukin, *et al.*, *Science* **347**, 1129 (2015).
- [27] S. Sangtawesin, B. L. Dwyer, S. Srinivasan, J. J. Allred, L. V. H. Rodgers, K. De Greve, A. Stacey, N. Dontschuk, K. M. O'Donnell, D. Hu, D. A. Evans, C. Jaye, D. A. Fischer, M. L. Markham, D. J. Twitchen, H. Park, M. D. Lukin, N. P. de Leon, *et al.*, *Phys. Rev. X* **9**, 031052 (2019).
- [28] A. Ariyaratne, D. Bluvstein, B. A. Myers, and A. C. B. Jayich, *Nat. Commun.* **9**, 2406 (2018).
- [29] M. W. Doherty, F. Dolde, H. Fedder, F. Jelezko, J. Wrachtrup, N. B. Manson, and L. C. L. Hollenberg, *Phys. Rev. B* **85**, 205203 (2012).
- [30] E. V. Oort and M. Glasbeek, *Chem. Phys. Lett.* **168**, 529 (1990).
- [31] M. Kim, H. J. Mamin, M. H. Sherwood, K. Ohno, D. D. Awschalom, and D. Rugar, *Phys. Rev. Lett.* **115**, 087602 (2015).
- [32] P. Jamonneau, M. Lesik, J. P. Tetienne, I. Alvizu, L. Mayer, A. Dréau, S. Kosen, J.-F. Roch, S. Pezzagna, J. Meijer, T. Teraji, Y. Kubo, P. Bertet, J. R. Maze, V. Jacques, *et al.*, *Phys. Rev. B* **93**, 024305 (2016).
- [33] M. H. Devoret, A. Wallraff, and J. M. Martinis, arXiv:0411174 (2004).
- [34] M. Brownnutt, M. Kumph, P. Rabl, and R. Blatt, *Rev. Mod. Phys.* **87**, 1419 (2015).
- [35] B. Christensen, C. Wilen, A. Opremcak, J. Nelson, F. Schlenker, C. Zimonick, L. Faoro, L. Ioffe, Y. Rosen, J. DuBois, *et al.*, arXiv:1905.13712 (2019).
- [36] A. V. Kuhlmann, J. Houel, A. Ludwig, L. Greuter, D. Reuter, A. D. Wieck, M. Poggio, and R. J. Warburton, *Nat. Phys.* **9**, 570 (2013).
- [37] A. Safavi-Naini, P. Rabl, P. F. Weck, and H. R. Sadeghpour, *Phys. Rev. A* **84**, 023412 (2011).
- [38] D. Bluvstein, Z. Zhang, and A. C. B. Jayich, *Phys. Rev. Lett.* **122**, 076101 (2019).

Supplemental Materials for “Fast relaxation on magnetic-dipole-forbidden spin transitions of nitrogen-vacancy centers in nanodiamonds”

A. Gardill,^{*} M. C. Cambria,^{*} and S. Kolkowitz[†]
Department of Physics, University of Wisconsin, Madison, Wisconsin 53706, USA

I. EXPERIMENTAL APPARATUS

Our apparatus consists of a room temperature confocal microscope with a 1.3 NA oil-immersion objective. Two signal generators were used to drive separate state selective π -pulses between $|0\rangle \leftrightarrow |+1\rangle$ and $|0\rangle \leftrightarrow |-1\rangle$. Software to control the experiment was built upon LabRAD.

II. NANODIAMOND SAMPLE PREPARATION

Nanodiamond solutions used in this paper were purchased from Adámas Nano (NDNV40nmLw10ml). The nanodiamonds were diluted in deionized (DI) water to a concentration of 10 $\mu\text{g}/\text{mL}$, then poly-vinyl alcohol (PVA) was added with a weight-to-weight (PVA to water) concentration of 0.17%. A gridded glass coverslip was cleaned with isopropyl alcohol and nanodiamond solution was spin coated onto the coverslip at 3000 rpm for 20 seconds. The nitrogen-vacancy centers (NVs) were imaged through the back side of the coverslip, with the nanodiamonds in air under ambient conditions.

All of the NVs presented in the main text were sampled from a single spin-coated glass coverslip. To verify that the noise we observe is not a result of the glass surface or of the PVA used in the solution, we measured a single NV deposited on a clean silicon wafer from a DI water/nanodiamond solution containing no PVA. The solution was dropped onto a clean silicon wafer and then heated on a hot-plate at 160°C to evaporate the water. Figure 1 shows a measurement of the relaxation rates of this NV at $\Delta_{\pm} = 13.9(6)\text{MHz}$, which shows $\gamma = 63(10)\text{kHz}$ and $\Omega = 0.17(3)\text{kHz}$, confirming the fast relaxation behavior we observe is intrinsic to the nanodiamonds.

III. NV SELECTION

Each NV presented in this paper was selected based on its second-order correlation function $g^{(2)}(\tau)$ and spin-dependent contrast. Figure 2 shows the $g^{(2)}(\tau)$ measurements of all five NVs used in this work. All 5 NVs exhibit a $g^{(2)}(0) < 0.5$ with no background subtraction, confirming that they are single photon emitters. We then

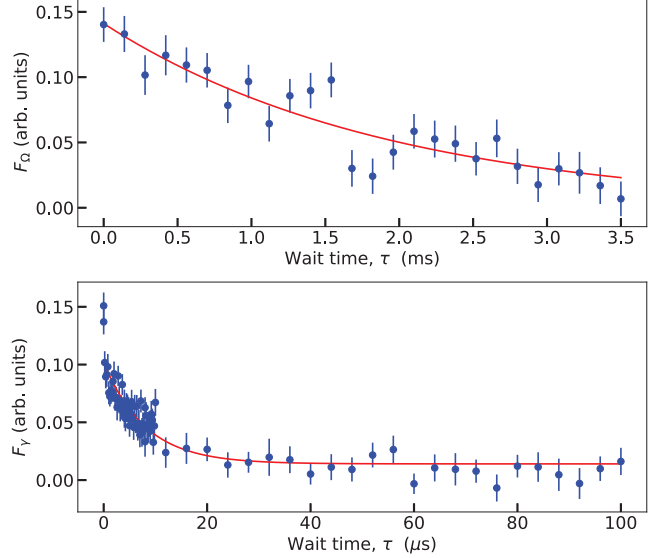


FIG. 1. Measurement of γ and Ω on a single NV in nanodiamond on a silicon substrate. Red lines are fits to Eqs. 3 and 4 from the main text, with rates $\gamma = 63(10)\text{kHz}$ and $\Omega = 0.17(3)\text{kHz}$. Error bars represent one standard error.

perform optically detected magnetic resonance (ODMR) to select for NVs with large spin-dependent fluorescence contrast ($\geq 10\%$ change in fluorescence). This bias in our selection process was necessary to achieve adequate signal-to-noise ratios in our relaxation measurements, and likely selects for larger nanodiamonds and/or NVs further from the surfaces of the nanodiamonds.

IV. POPULATION DYNAMICS

Here we consider the rate equations for the population dynamics of a generic three level system. There are three possible transitions between states: the $|-1\rangle \leftrightarrow |+1\rangle$ transition with rate γ , the $|0\rangle \leftrightarrow |+1\rangle$ transition with rate Ω_+ , and the $|0\rangle \leftrightarrow |-1\rangle$ transition with rate Ω_- . Figure 3 shows measurements of Ω_+ and Ω_- on NV1 at two different splittings, $\Delta_{\pm} = 28.9(6)\text{MHz}$ and $\Delta_{\pm} = 1016.8(6)\text{MHz}$. The measured values of Ω_+ and Ω_- agree to within error at both splittings, and we take $\Omega_+ = \Omega_- \equiv \Omega$ for all the splittings considered in this paper ($\sim 10 - 1000\text{MHz}$). This assumption was consistent with all of our measurements on all of the NVs in this work. The reported values of Ω are measured on the $|0\rangle \leftrightarrow |+1\rangle$ transition. The system of equations describing the change of

^{*} These authors contributed equally.

[†] kolkowitz@wisc.edu

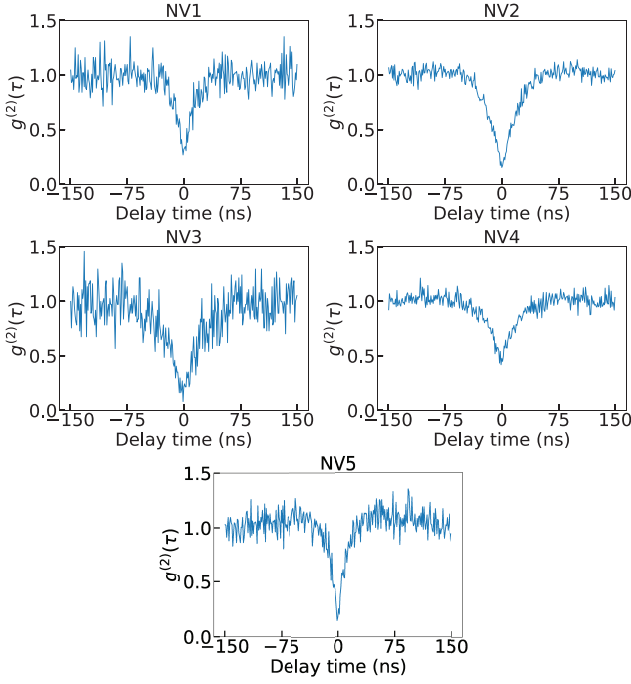


FIG. 2. Second-order photon correlation function ($g^{(2)}(\tau)$) measurements of the five NVs presented in this paper, with no background subtraction. The $g^{(2)}(0)$ values for the NVs are: NV1: 0.319, NV2: 0.153, NV3: 0.216, NV4: 0.476, NV5: 0.180.

population ρ_i in state $|i\rangle$ is

$$\frac{d}{dt} \begin{pmatrix} \rho_0 \\ \rho_{+1} \\ \rho_{-1} \end{pmatrix} = \begin{pmatrix} -2\Omega & \Omega & \Omega \\ \Omega & -\Omega - \gamma & \gamma \\ \Omega & \gamma & -\Omega - \gamma \end{pmatrix} \begin{pmatrix} \rho_0 \\ \rho_{+1} \\ \rho_{-1} \end{pmatrix}. \quad (1)$$

Requiring that $\rho_0(\tau) + \rho_{+1}(\tau) + \rho_{-1}(\tau) = 1$ and setting the initial condition $\rho_i(0)$ results in the population dynamics given by Eqs. 1 and 2 in the main text.

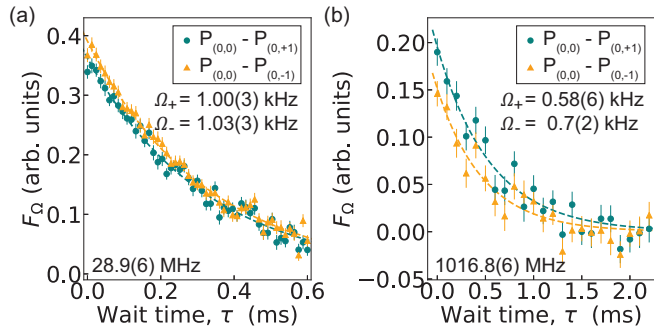


FIG. 3. Comparison of Ω_+ and Ω_- for NV1 at two different splittings. Both $P_{0,0} - P_{0,+1}$ (teal circles) and $P_{0,0} - P_{0,-1}$ (orange triangles) are plotted with single exponential fits (dashed lines) to determine Ω_+ and Ω_- , which agree to within error. Error bars represent one standard error. Reported error on Δ_{\pm} and Ω_{\pm} is twice the standard error. (a) NV1 at $\Delta_{\pm} = 28.9(6)$ MHz. (b) NV1 at $\Delta_{\pm} = 1016.8(6)$ MHz.

V. COMPLETE SET OF RELAXATION MEASUREMENTS

The ability to prepare and readout in any of the three NV spin states allows for a total of nine possible relaxation measurements. To confirm our model, we performed all nine possible measurements on the same NV with the same applied magnetic field, as shown in Fig. 4. The population dynamics for all 9 possible combinations are well described by the population dynamics given by Eqs. 1 and 2 in the main text after accounting for π -pulse infidelities, as discussed below in Sec. VII. We denote the normalized fluorescence of a relaxation measurement with initialization into $|i\rangle$ and readout of $|j\rangle$ by $P_{i,j}$. The data was normalized such that zero corresponds to $P_{+1,-1}(\tau = 0)$ and unity corresponds to $P_{0,0}(\tau = 0)$.

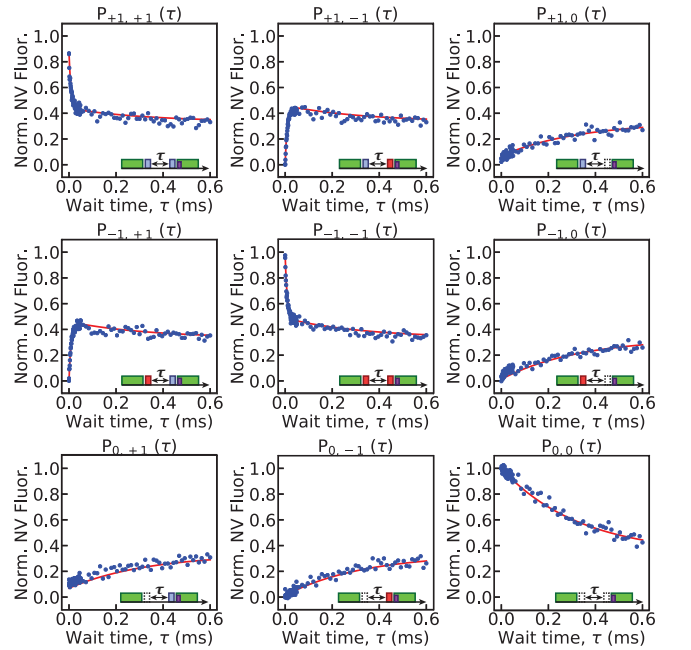


FIG. 4. Example of all 9 measurements made possible by the ability to prepare and readout in any of the three NV states. These measurements were conducted at $\Delta_{\pm} = 28.9(6)$ MHz. Red lines are Eqs. 2 and 3, with $\epsilon_+ = 6.9\%$, $\epsilon_- = 1.3\%$, $\Omega = 1.0$ kHz, and $\gamma = 56$ kHz.

VI. PROTOCOL FOR EXTRACTING THE RATES γ AND Ω

To extract γ and Ω , we take the difference between measured population decay curves and fit to the result with the single exponential functions F_{Ω} and F_{γ} defined in Eqs. 3 and 4 of the main text. At each value of Δ_{\pm} , we measure $P_{+1,+1}$, $P_{+1,-1}$, $P_{0,+1}$, and $P_{0,0}$, with $P_{+1,+1}$ and $P_{+1,-1}$ measured on two timescales in order to sufficiently resolve the fast $|-1\rangle \leftrightarrow | +1\rangle$ relaxation. Figure 5 shows representative data for F_{Ω} and F_{γ} . Table I shows

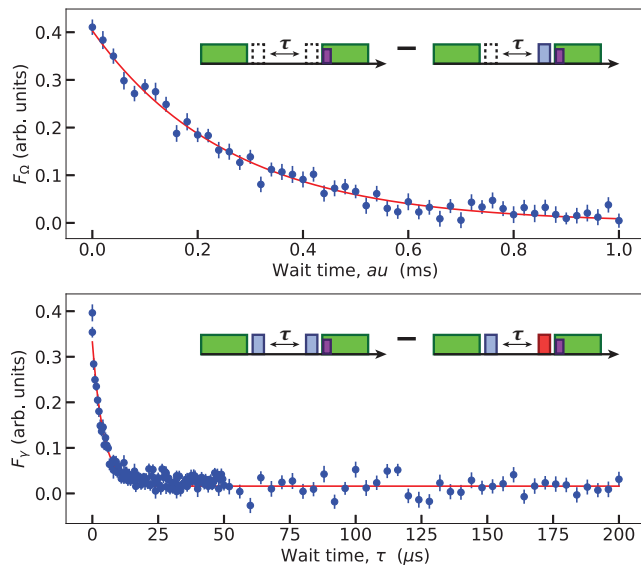


FIG. 5. Representative data from NV1 showing subtraction of relaxation signals to extract Ω and γ , where red lines are fits to Eqs. 3 and 4 from the main text. The splitting is $\Delta_{\pm} = 19.8(6)$ MHz and the rates extracted are $\Omega = 1.28(8)$ and $\gamma = 117(8)$ kHz. Error bars are one standard error.

all the rates measured for this paper. The measurements for all 5 NVs were recorded in pseudo-random order to avoid conflating temporal effects with dependence on Δ_{\pm} .

VII. MICROWAVE π -PULSE INFIDELITIES

In order to fit the population decay curves shown in Figs. 1 and 2 of the main text and Fig. 4 of the supplement, imperfections in the microwave π -pulses used to prepare and readout the populations must be taken into account. The fraction of population not transferred by the π_{\pm} -pulse is denoted ϵ_{\pm} . The modified equations for reading out the population of $|+1\rangle$, $|-1\rangle$, and $|0\rangle$ after initializing in $|+1\rangle$ are

$$\begin{aligned}
 P'_{+1,\pm 1}(\tau) &= \frac{1}{3} \pm \left[\frac{1}{2}(1 - \epsilon_{+})e^{-(2\gamma + \Omega)\tau} \right] (1 - \epsilon_{\pm}) \quad (2) \\
 &\quad - \left[\frac{1}{2}(\epsilon_{+} - \frac{1}{3})e^{-3\Omega\tau} \right] (1 - \epsilon_{\pm}) \\
 &\quad + \left[(\epsilon_{+} - \frac{1}{3})e^{-3\Omega\tau} \right] \epsilon_{\pm}, \\
 P'_{+1,0}(\tau) &= \frac{1}{3} + (\epsilon_{+} - \frac{1}{3})e^{-3\Omega\tau}. \quad (3)
 \end{aligned}$$

These equations are used to produce the dashed colored lines in Figs. 1 and 2 of the main text, with $\epsilon_{+} = 6.9\%$ and $\epsilon_{-} = 1.3\%$. The infidelities were calculated as the relative decrease in contrast in the measured Rabi signal over one π -pulse.

If we include the effect of π -pulse infidelities on F_{Ω} and F_{γ} , then we obtain the modified equations

$$F'_{\Omega} = (1 - \epsilon_{+})e^{-3\Omega\tau}, \quad (4)$$

$$\begin{aligned}
 F'_{\gamma} &= \left(1 - \frac{1}{2}(\epsilon_{+} + \epsilon_{-}) \right) (1 - \epsilon_{+})e^{-(2\gamma + \Omega)\tau} \quad (5) \\
 &\quad + \frac{3}{2}(\epsilon_{+} - \epsilon_{-}) \left(\epsilon_{+} - \frac{1}{3} \right) e^{-3\Omega\tau}.
 \end{aligned}$$

The differential protocol described in Sec. VI for the extraction of the rates γ and Ω is relatively insensitive to π -pulse infidelities, so they were not included in the analysis in order to simplify the procedure. However, if the difference between the infidelities ϵ_{+} and ϵ_{-} is significant, then F'_{γ} will not decay to zero on the $(2\gamma + \Omega)$ timescale, resulting in an apparent offset. This was observed in some of our measurements where $\gamma \gg \Omega$. In these cases we account for the discrepancy by adding a fixed offset to F_{γ} . This offset is not a free parameter of the fit, but is instead calculated as the average difference in the subtracted data after $\sim 3 \times$ the time constant $1/(2\gamma + \Omega)$.

VIII. ERROR ANALYSIS

An individual data point in a relaxation measurement $P_{i,j}$ is the average of $\sim 10 - 100$ runs each consisting of $\sim 10^5$ repetitions of the same measurement sequence. Each run produces a single value which is the cumulative total of the counts recorded over the measurement sequence repetitions. The standard error of each data point is taken with respect to the runs. The fits to F_{Ω} and F_{γ} are weighted by the standard errors on the data points, and the errors on Ω and γ are propagated from the standard errors of the fits to F_{Ω} and F_{γ} .

IX. DATA FOR NV5

Figure 6 shows the measured values of γ and Ω for NV5 (which were not plotted in the main text due to space constraints). This NV had the lowest spin-dependent fluorescence contrast ($\sim 10\%$) which, in combination with imperfect alignment of the applied magnetic field, prohibited us from making measurements at splittings greater than ~ 240 MHz.

X. TEMPORAL FLUCTUATIONS OF γ FOR NV1

Figure 4 in the main text presents temporal fluctuations of the rate γ for NV2 at $\Delta_{\pm} \approx 29$ MHz. We performed the same measurement on NV1 at $\Delta_{\pm} \approx 26$ MHz and observed similar fluctuations. Figure 7(a) shows consecutive measurements performed on NV1 at the same splitting over ~ 65 hours. The inset histogram shows the

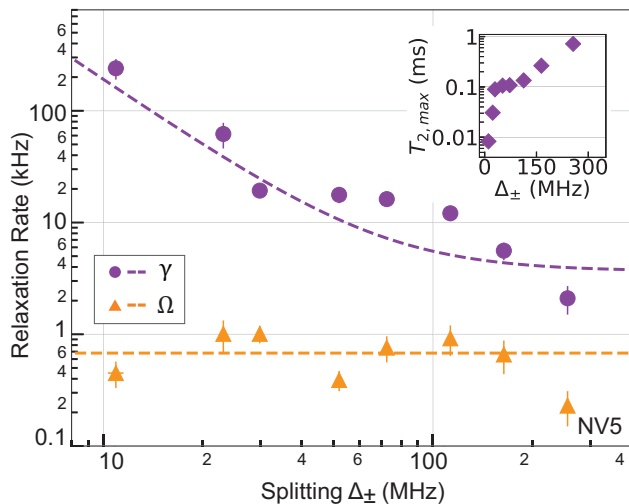


FIG. 6. Dependence of the relaxation rates of NV5 on the frequency splitting between $|\pm 1\rangle$ states, Δ_{\pm} . Purple circles represent measurement of γ and orange triangles represent measurement of Ω . A fit of $\gamma(\Delta_{\pm}) = A_0/\Delta_{\pm}^2 + \gamma_{\infty}$ is shown as purple dashed line. Inset shows the corresponding maximum achievable T_2 (purple diamonds) on a semi-log plot. Error bars are twice the standard error.

distribution of the measured rates along with a Gaussian curve of standard deviation equal to the average standard error of a single measurement. It is clear that the spread of the measured rates is larger than the average uncertainty of the measurements. Figure 7(b) compares the population decay curves for two adjacent measured rates, showing that the observed fluctuations in γ are above our signal-to-noise ratio.

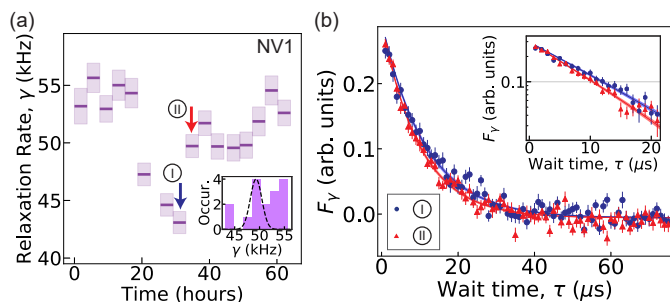


FIG. 7. Temporal fluctuations in γ observed in NV1. (a) Rate γ at a single splitting $\Delta_{\pm} \approx 26$ MHz measured over 65 hours. Error bars are one standard error. Inset shows histogram of measured rates overlaid with a Gaussian curve with standard deviation equal to the average standard error of the measurements. (b) Subtraction curves F_{γ} for adjacent measurements in (a). Inset shows first 20 μs of same data plotted on a semi-log scale. Error bars are one standard error, shaded error on fit represents one standard error of the extracted γ .

XI. EXCLUSION OF ALTERNATIVE EXPLANATIONS FOR FAST MAGNETICALLY FORBIDDEN RELAXATION

Here we consider and rule out two alternative explanations for the fast magnetic-dipole-forbidden relaxation γ that we observe. Namely, we examine the effect of slowly varying off-axis fields mixing the spin eigenstates, and the effect of magnetic field noise on eigenstates mixed by static off-axis fields.

We first consider the possibility that eigenstate mixing due to slowly varying off-axis strain, electric, or magnetic fields is responsible for the observed relaxation. We find that in order to significantly affect the composition of the eigenstates, the fields would also significantly shift the ODMR resonance frequencies in time. As the ODMR resonances were stable relative to their linewidths on the timescale of all of our measurements, we conclude that state mixing alone cannot explain the observed fast relaxation.

We next investigate the effect of magnetic field noise on statically mixed eigenstates. If the energy eigenstates are eigenstates of S_z , then the $|-1\rangle \leftrightarrow | +1\rangle$ transition is magnetically forbidden, and the observed fast relaxation cannot be attributed to magnetic field noise. However, in the presence of off-axis fields, the energy eigenstates are not eigenstates of S_z . To distinguish between the S_z eigenstates and the energy eigenstates, we denote the S_z eigenstate with spin projection m_s by $|S_z; m_s\rangle$ and the energy eigenstate with majority component $|S_z; m_s\rangle$ by $|H; m_s\rangle$. In this case, γ is the relaxation rate on the $|H; -1\rangle \leftrightarrow |H; +1\rangle$ transition.

If we treat magnetic field noise as a harmonic perturbation and account for the anisotropy in the effect of the noise by averaging over the possible noise field orientations, then γ_B , the first-order $|H; -1\rangle \leftrightarrow |H; +1\rangle$ relaxation rate due to magnetic field noise, obeys

$$\gamma_B \propto \overline{\langle H; -1 | H_B | H; +1 \rangle^2}, \quad (6)$$

where H_B is the perturbative magnetic Hamiltonian (Eq. 7 in the main text) and $\overline{}$ denotes the average of all possible orientations. Similarly, $\Omega_{B,\pm}$, the first-order $|H; 0\rangle \leftrightarrow |H; \pm 1\rangle$ relaxation rate due to magnetic noise obeys

$$\Omega_{B,\pm} \propto \overline{\langle H; 0 | H_B | H; \pm 1 \rangle^2}. \quad (7)$$

The $|H; -1\rangle \leftrightarrow |H; +1\rangle$ transition is magnetically forbidden if there is no off-axis magnetic or electric/scaled strain field. In our experiment, off-axis magnetic field is present due to imperfect alignment of the applied d.c. field with the NV axis, and off-axis electric/strain field is intrinsic to the nanodiamonds we studied. Both of these effects could contribute to a nonzero γ_B .

In order to determine whether the observed $|H; -1\rangle \leftrightarrow |H; +1\rangle$ relaxation is attributable to magnetic field noise, we compare the ratio of Ω and γ where $\Delta_{0,-1}$, the splitting between $|H; 0\rangle$ and $|H; -1\rangle$, is on the same order

of magnitude as $\Delta_{-1,+1}$, the splitting between $|H; -1\rangle$ and $|H; +1\rangle$. In this case, we expect that the magnetic noise power at frequency $\Delta_{-1,+1}$ is on the same order of magnitude as the magnetic noise power at frequency $\Delta_{0,-1}$. We conducted this comparison on NV1 with $\Delta_{0,-1} = 2438$ MHz and $\Delta_{-1,+1} = 1017$ MHz. This data is marked with an asterisk in Table I. With Eqs. 6 and 7, we calculate the ratio of $\Omega_{B,-}$ and γ_B to be ~ 25 if we assume that the magnetic noise power is the same at $\Delta_{-1,+1}$ and $\Delta_{0,-1}$. We measure $\Omega = 0.7(2)$ kHz on the $|H; 0\rangle \leftrightarrow |H; -1\rangle$ transition (see Fig. 3) and $\gamma = 0.41(10)$ kHz. The ratio between these two rates is ~ 2 , or more than an order of magnitude below what would be expected if magnetic noise were the dominant source of relaxation. We therefore conclude that magnetic noise is not a significant source of $|H; -1\rangle \leftrightarrow |H; +1\rangle$ relaxation.

In addition, in order to further test our hypothesis that the fast relaxation we observe is not a result of a nonzero γ_B due to eigenstate mixing, we performed measurements on two of the NVs (NV1 and NV2) with intentionally misaligned magnetic fields with respect to the NV axis, and at zero applied magnetic field for three of the NVs (see Table I). In all cases we found that the rate γ depended only on the splitting Δ_{\pm} , and was independent of θ_B and the amplitude of the applied magnetic field $|\mathbf{B}|$.

XII. CONSIDERATION OF BRIGHT AND DARK STATES

Due to off-axis electric/strain field intrinsic to the nanodiamonds, in the limit of low applied magnetic fields

the spin eigenstates are the bright and dark states $|\pm\rangle = (|+1\rangle \mp e^{-i\phi_{\pi\pm}} |-1\rangle) / \sqrt{2}$, as defined in the main text. Here we show that the same population equations and arguments used to analyze the $\{|0\rangle, |-1\rangle, |+1\rangle\}$ eigenstates can also be applied to the $\{|0\rangle, |-\rangle, |+\rangle\}$ eigenstates. For the $\{|0\rangle, |-\rangle, |+\rangle\}$ three-level system, γ is generalized to describe the transition rate between $|-\rangle$ and $|+\rangle$. Likewise, Ω_- describes the $|0\rangle \leftrightarrow |-\rangle$ transition rate and Ω_+ describes the $|0\rangle \leftrightarrow |+\rangle$ transition rate. The $|0\rangle \leftrightarrow |\pm\rangle$ transition is electrically forbidden, but magnetically allowed; we calculate $\Omega_{B,+}/\Omega_{B,-} = 1$ using Eq 7, in agreement with our observation that $\Omega_+ \approx \Omega_-$ and our decision to use the single-valued Ω for both Ω_+ and Ω_- .

We further find that the $|-\rangle \leftrightarrow |+\rangle$ and $|-1\rangle \leftrightarrow |+1\rangle$ transitions are similarly affected by electric/strain noise. Neither the $|-1\rangle \leftrightarrow |+1\rangle$ transition nor the $|-\rangle \leftrightarrow |+\rangle$ transition can be driven by axial electric/strain field, but both can be driven by off-axis electric/strain fields. As a point of contrast, the $|-\rangle \leftrightarrow |+\rangle$ transition is anisotropically sensitive to off-axis electric/strain noise, while the $|-1\rangle \leftrightarrow |+1\rangle$ transition is isotropically sensitive to the same noise. If, by analogy to equation 6, we define γ_{Π} as the rate of $|-\rangle \leftrightarrow |+\rangle$ or $|-1\rangle \leftrightarrow |+1\rangle$ relaxation attributable to electric/strain noise, then we calculate γ_{Π} for the $|-\rangle \leftrightarrow |+\rangle$ transition to be half of γ_{Π} for the $|-1\rangle \leftrightarrow |+1\rangle$ transition, showing that the bright and dark states and the $|\pm 1\rangle S_z$ eigenstates are similarly susceptible to relaxation due to off-axis electric/strain noise.

TABLE I. Complete set of relaxation rates presented in this work. Reported uncertainty is twice the standard error. The angle θ_B is the estimated angle of the applied magnetic field with respect to the NV axis. This value is calculated numerically from the NV resonances as the applied magnetic field is increased with a fixed orientation. Measurements taken in absence of applied magnetic field are not assigned θ_B . *This measurement is used as evidence against magnetic noise driving transitions between $|\pm 1\rangle$, as discussed in section XI.

NV1				NV2			
Δ_{\pm} (MHz)	Ω (kHz)	γ (kHz)	θ_B (deg)	Δ_{\pm} (MHz)	Ω (kHz)	γ (kHz)	θ_B (deg)
19.5(6)	0.83(8)	58(3)	n/a	15.3(6)	0.24(2)	124(6)	n/a
19.8(6)	1.28(8)	117(8)	37	29.1(6)	0.41(2)	20.9(6)	32
27.7(6)	1.30(12)	65(3)	37	29.2(6)	0.33(3)	31.1(8)	64
28.9(6)	1.00(3)	56(3)	37	44.8(6)	0.36(2)	6.4(2)	32
32.7(6)	1.42(10)	42.6(18)	37	45.5(6)	0.27(2)	8.5(2)	64
51.8(6)	1.85(16)	13.1(4)	37	56.2(6)	0.326(16)	3.64(16)	32
97.8(6)	1.41(10)	3.9(2)	37	56.9(6)	0.42(10)	3.77(18)	32
116.0(6)	1.18(12)	4.7(2)	37	85.2(6)	0.29(2)	2.62(10)	64
268.0(6)	1.04(8)	2.0(2)	37	101.6(6)	0.312(18)	1.33(10)	32
350.0(6)	0.72(8)	1.6(2)	58	280.4(6)	0.28(2)	0.44(3)	64
561.7(6)	1.19(12)	0.70(10)	37	697.5(6)	0.29(4)	0.81(12)	64
1016.8(6)*	0.58(6)	0.41(10)	37				
NV3				NV4			
Δ_{\pm} (MHz)	Ω (kHz)	γ (kHz)	θ_B (deg)	Δ_{\pm} (MHz)	Ω (kHz)	γ (kHz)	θ_B (deg)
17.1(6)	0.7(3)	110(20)	51	23.4(1)	0.28(3)	35(3)	n/a
28.6(6)	0.53(10)	90(10)	51	26.2(6)	0.33(6)	29(2)	9
53.0(6)	0.87(18)	26.2(18)	51	36.2(6)	0.32(6)	20.3(10)	9
81.2(6)	1.7(4)	17.5(12)	51	60.5(6)	0.24(4)	9.1(6)	9
128.0(6)	0.60(10)	11.3(8)	51	48.1(6)	0.31(2)	15.8(6)	9
283.1(6)	0.70(14)	5.6(6)	51	92.3(6)	0.25(2)	6.4(2)	9
495.8(6)	1.4(8)	3.7(8)	51	150.8(1)	0.29(4)	4.1(3)	9
746.0(6)	1.0(3)	2.8(6)	51	329.6(6)	0.33(4)	1.23(14)	9
				884.9(6)	0.29(4)	0.45(6)	9
				1080.5(6)	0.28(10)	0.7(2)	9
				1148.4(6)	0.38(8)	0.35(6)	9
NV5							
Δ_{\pm} (MHz)	Ω (kHz)	γ (kHz)	θ_B (deg)				
10.9(6)	0.45(12)	240(50)	71				
23.1(6)	1.0(3)	62(16)	71				
29.8(6)	1.01(18)	19(2)	71				
51.9(6)	0.39(8)	18(3)	71				
72.4(6)	0.8(2)	16(2)	71				
112.9(6)	0.9(3)	12.1(18)	71				
164.1(6)	0.7(2)	5.6(10)	71				
256.2(6)	0.23(8)	2.1(6)	71				